Available online at www.sciencedirect.com

ScienceDirect

Trans. Nonferrous Met. Soc. China 33(2023) 3083−3099

Transactions of
Nonferrous Metals
Society of China

www.tnmsc.cn

Evaluation of tensile property and strengthening mechanism of molybdenum alloy bars doped with different ultrafine oxides

Liu-jie XU[1,2], Tie-long SUN[1], Yu-cheng ZHOU[2], Zhou LI[3], Shi-zhong WEI[1]

1. Henan Key Laboratory of High-temperature Structural and Functional Materials,
Henan University of Science and Technology, Luoyang 471003, China;
2. National Joint Engineering Research Center for Abrasion Control and Molding of Metal Materials,
Henan University of Science and Technology, Luoyang 471003, China;
3. Beijing National Innovation Institute of Lightweight Ltd.,
China Academy of Machinery Science and Technology, Beijing 100089, China

Received 7 April 2022; accepted 5 December 2022

Abstract: Three kinds of molybdenum alloy are doped with 2.0 wt.% different ultrafine oxide particles (Al_2O_3, ZrO_2 and La_2O_3) via hydrothermal synthesis, co-precipitation, co-decomposition, powder metallurgy, and rotary swaging. Three nano-oxides refine molybdenum grains by more than 70% and change the fracture modes from brittle fracture to ductile fracture, thereby dramatically improving the integrated mechanical properties of the alloys. Moreover, the trade-off between strength and ductility is offset. Mo−ZrO_2 alloy has the highest strength and plasticity, which is attributed to fine ZrO_2 particles and a semi-coherent interface between ZrO_2 and molybdenum matrix. Moreover, a quantitative strengthening model correlating dislocation density, oxide volume fraction and size, and molybdenum grain size is established.

Key words: molybdenum alloy; Al_2O_3; ZrO_2; La_2O_3; strength−elongation product; strengthening model

---

1 Introduction

Molybdenum (Mo) has been widely used in high-temperature fields such as nuclear industry, aerospace and metallurgy because of its high melting point (2610 °C), low thermal expansion coefficient, large elastic modulus and excellent high-temperature mechanical properties [1,2]. Some of the key mechanical properties of Mo alloys are strength, ductility, fracture toughness, and creep resistance at elevated temperatures, which are required in structural materials [3−5]. However, pure molybdenum, which has single-phase microstructure, cannot simultaneously meet these requirements. Fabricating multiphase molybdenum alloy is an effective way to ensure balance between strength and ductility.

Over the past few decades, to improve the mechanical property of pure molybdenum, multiphase molybdenum alloys, such as Mo−Re, Mo−Hf−C, Mo−Ti−Zr (TZM) alloy, oxide-particle-dispersed Mo (ODS-Mo) alloys, have been developed [6−9]. Traditionally, increase in strength is always accompanied by decrease in ductility. TZM alloys, as high-performance multiphase molybdenum alloys, have high strength and hardness compared with pure molybdenum [10,11]. However, their elongation after fracture at room temperature is usually less than 10%. Hence, offsetting the trade-off between strength and ductility is difficult.

Corresponding author: Tie-long SUN, Tel: +86-18848961112, E-mail: tie_long@163.com

DOI: 10.1016/S1003-6326(23)66319-8

ODS-Mo alloys not only have high strength but also have good plasticity. When oxide particles are coarse, they are mainly located at the grain boundary of Mo and weaken the interfacial bonding force between oxide particles and Mo matrix, resulting in intergranular fracture [12]. JIANG et al [13] found that when precipitated phase is sufficiently small, the degree of dispersion of precipitated phase in matrix is large, and the mechanical properties of alloy are significantly improved. Therefore, reducing the size of oxide particle is essential to improving the mechanical properties of ODS-Mo alloys. SILVA et al [14] analyzed the particle-induced nucleation of industrial MZ-17 (Mo−1.7%ZrO_2) alloy recrystallization and pointed out that the addition of ZrO_2 particles significantly improved the recrystallization temperature and high-temperature mechanical properties by refining grains and hindering dislocation movement. Ultrafine La_2O_3-, CeO_2-, or Y_2O_3-doped molybdenum alloys prepared by powder metallurgy showed high strength and excellent ductility due to characteristics of rare earth oxides [12,15,16]. However, in high-temperature sintering process (usually over 1850 °C), these fine rare earth oxide particles in molybdenum agglomerate due to high chemical activity, which worsens the mechanical properties of alloys. Given that ceramic oxides (Al_2O_3 and ZrO_2) have higher economy and compatibility with molybdenum matrices than rare earth oxides, we prepared Mo−Al_2O_3 and Mo−ZrO_2 alloys by the powder metallurgy method; good strengthening effect was obtained [17−19]. However, few studies explored the systematicness of differences among molybdenum alloys doped with different oxides. To clarify the enhancing effects of different oxides as strengthening phases, we fabricated three kinds of molybdenum alloys by doping with different ultrafine oxide particles (La_2O_3, Al_2O_3, and ZrO_2), aiming to offset the trade-off between strength and ductility. The research would be helpful for understanding the different and similar effects of different strengthening phases on the microstructures and mechanical properties of metal materials.

2 Experimental

2.1 Preparation of samples

Three molybdenum alloy powders doped with different oxides (Al_2O_3, ZrO_2, La_2O_3) and one pure molybdenum powder were designed and prepared via hydrothermal synthesis and two-step hydrogen reduction methods [20]. The volume fraction of each doped oxide was 2.0%. A mixed solution of $(NH_4)_2Mo_4O_{13}\cdot 2H_2O$ and nitric acid (pH=1) was placed in a 500 mL stainless steel autoclave and heated at 170 °C for 15 h for the preparation of a MoO_3 suspension liquid. Under the same condition, a mixed solution of nitrates $Al(NO_3)_3\cdot 9H_2O$, $La(NO_3)_3\cdot 6H_2O$, $Zr(NO_3)_4\cdot 5H_2O/Y(NO_3)_3\cdot 6H_2O$ ($[Zr^{4+}]:[Y^{3+}]$ in a molar ratio of 88:12), and urea (pH=9) were used in preparing the suspensions of corresponding oxides. The two suspensions were mixed, stirred, and filtered. After drying at 90 °C, the precursors of molybdenum/oxide powder were obtained. Then, the precursors were converted into molybdenum alloy powder by calcination and two-stage hydrogen reduction (75% H_2 and 25% N_2). The reduced powders were filled in a rubber mold for the preparation of a composite blank with *d*20 mm × 300 mm by cold isostatic pressing (280 MPa, 15 min). Finally, the molybdenum alloy rods with diameters of 8 mm were obtained by pressure-less sintering (1920 °C, 3 h), multistep swaging (1400 °C), and surface polishing. The total deformation from sintering (*d*20 mm) to final forging (*d*8 mm) was over 84%. The whole process of sample preparation is illustrated in Fig. 1. Pure Mo was prepared by the same method.

2.2 Characterization

The room temperature tensile samples of molybdenum alloys were obtained by machining, and the sizes of the sample are shown in Fig. 2. Before the tensile test, half of the samples placed in a molybdenum wire vacuum sintering furnace (ZMY−50−15) were annealed at 1200 °C for 1 h, and then the tensile properties were compared with those of the other half that were not subjected to annealing. The tensile test was carried out on a precision universal material testing machine (AG−I 250 kN) at a constant strain rate of $6.67\times10^{-4}\ s^{-1}$. Three samples were tested for each kind of materials, and the average values of ultimate tensile strength and elongation were calculated. Yield strength (YS) was determined by an offset method at 0.2% plastic strain according to the engineering stress–strain curves. The microstructure was observed with the Tescan VEGA3 SBH scanning

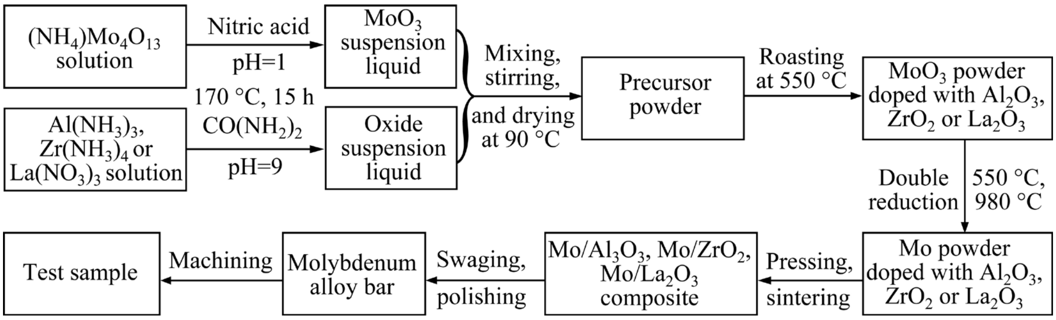

Fig. 1 Preparing process of test samples

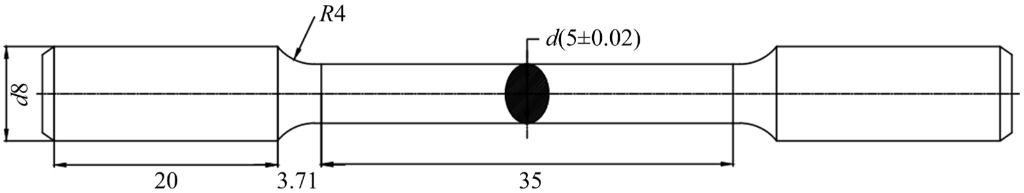

Fig. 2 Tensile sample at room temperature (Unit: mm)

electron microscopy (SEM) system equipped with an energy dispersive X-ray analysis system, JSM−5610LV field emission scanning electron microscopy (FESEM) system, and JEM−2100 transmission electron microscopy (TEM/HRTEM) system.

An X-ray diffraction (XRD) system (BRUX D 8) was used in analyzing the phase composition and distribution of molybdenum alloy. Vickers microhardness measurement was conducted on a Mitutoyo MH-3 hardness tester with a load of 1.98 N and dwell time of 10 s. The average size of alloy powder was measured in an alcohol medium with an OMCC LS−909 laser particle size analyzer. The nano-hardness and elastic modulus were analyzed under an application depth of 2000 nm, strain rate of 5 mN/s, allowable drift rate of 0.9 nm/s, and the residence time of 10 s by using a Keysight G200 friction indenter system equipped with Berkovich indenter. All studies on alloy microstructure were based on the cross-section of the rod vertical to the rotary swagging direction.

2.3 Calculation

The dislocation density of the alloy was determined using the XRD line broadening analysis and calculated via the Williamson–Smallman equation expressed as Eq. (1) [21]. The distribution value of dislocation density was estimated by using this equation:

$$\rho=\frac{2\sqrt{3}\varepsilon}{b\cdot d} \tag{1}$$

where ρ is the dislocation density, ε is the micro-strain, b is the magnitude of Burger vector with value of 2.72×10^{-10} m ($a/2\langle111\rangle$), and d is the crystallite size. The d and ε values were estimated using the Williamson–Hall equation according to the XRD peak broadening by using Eq. (2) [22]:

$$\delta_\mathrm{s}\cos\theta=\frac{C\lambda}{d}+\left(4\varepsilon\cdot\sin\theta\right) \tag{2}$$

where θ is the Bragg diffraction angle, C is a constant (~0.9), λ is the wavelength of Cu K_α, and δ_s is the structure broadening. The Bragg's diffraction peaks were fitted by means of the Voigt function from which θ and δ_s for each peak were obtained. The values of ε and d were determined as the slope and y-intercept of linear profile fit of the $\delta_\mathrm{s}\cos\theta$–$4\sin\theta$ plot, respectively.

3 Results and discussion

3.1 Analysis of powders

Figure 3 shows the SEM images and the corresponding XRD patterns of hydrothermal products with different raw materials heated at 170 °C for 15 h. Figure 3(a) shows the nanosheet morphology of $(NH_4)_2Mo_4O_{13}\cdot2H_2O$ hydrothermal products with an average length or width of 1−2 μm and a thickness of less than 100 nm. The X-ray

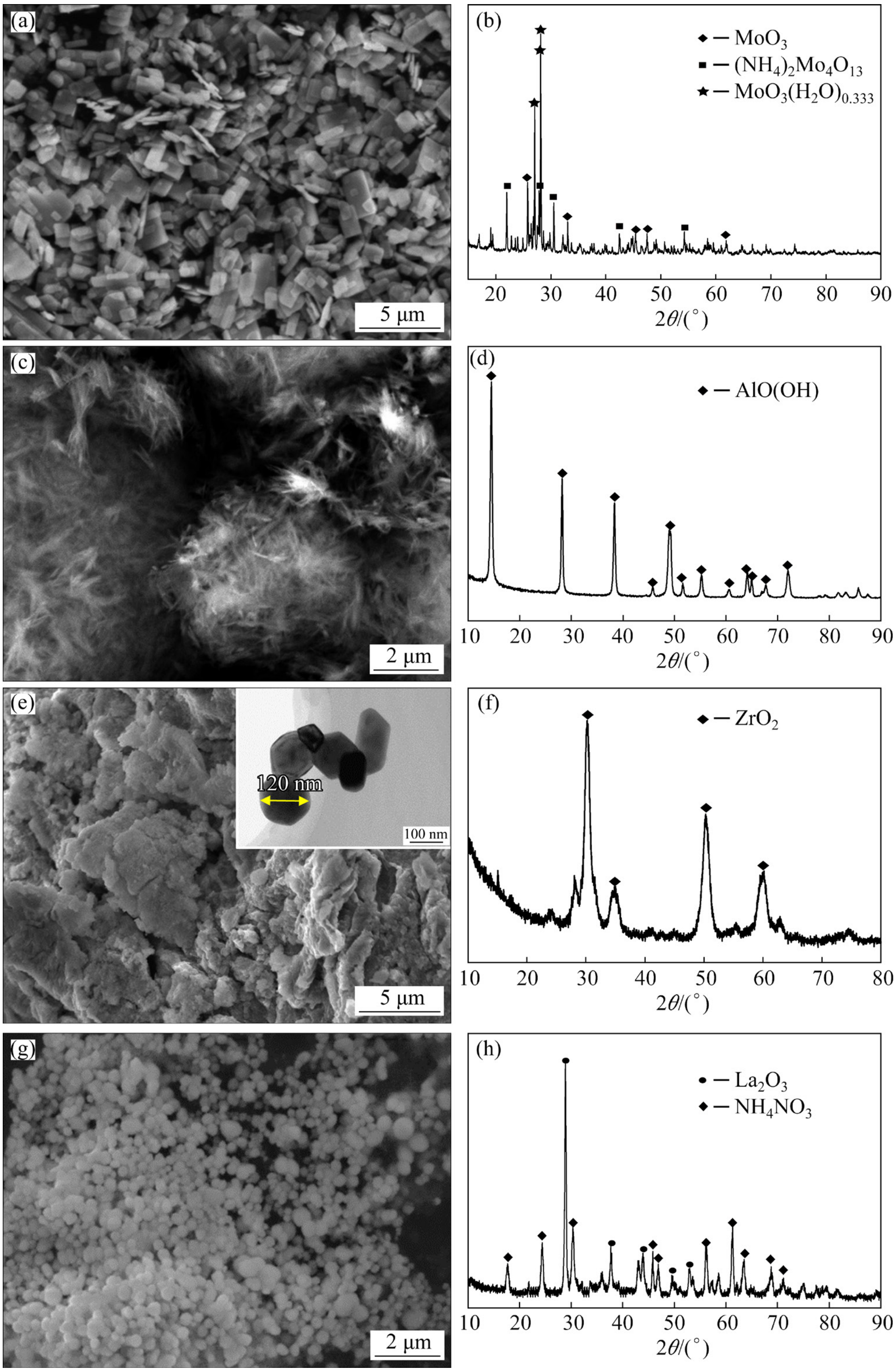

Fig. 3 SEM images (a, c, e, g) and corresponding XRD patterns (b, d, f, h) of hydrothermal products with different raw materials: (a, b) $(NH_4)_2Mo_4O_{13}\cdot 2H_2O$; (c, d) $Al(NO_3)_3\cdot 9H_2O$; (e, f) $Zr(NO_3)_4\cdot 5H_2O$; (g, h) $La(NO_3)_3\cdot 6H_2O$

diffraction patterns of the products can be attributed to $MoO_3(H_2O)_{0.333}$, MoO_3, and incompletely-decomposed $(NH_4)_2MoO_{13}$, as shown in Fig. 3(b). Figure 3(c) shows that the hydrothermal product of $Al(NO_3)_3\cdot 9H_2O$ is flocculent, and the phase of AlO(OH) can be determined by the XRD diffraction pattern (Fig. 3(d)). The large lumpy agglomerations of $Zr(NO_3)_4\cdot 5H_2O$ hydrothermal products are composed of ultrafine nanoparticles with a size of less than 120 nm, as seen in the inset of Fig. 3(e), and all the peaks of the corresponding XRD pattern correspond to ZrO_2 (Fig. 3(f)). Figure 3(g) shows the SEM image of $La(NO_3)_3\cdot 6H_2O$ hydrothermal products. The corresponding XRD pattern shows that the nanospheres with size of 100−400 nm are La_2O_3 (Fig. 3(h)).

Meanwhile, the XRD diffraction peaks of NH_4NO_3 can be indexed, and may be attributed to excessive urea. According to the SEM and XRD results, the possible reaction equations of hydrothermal process are as follows (Eqs. (3)−(6)):

$$(NH_4)_2Mo_4O_{13}\cdot 2H_2O+2HNO_3= \\ MoO_3+3Mo_3(H_2O)_{0.333}+2NH_3+2NO_2+3H_2O \tag{3}$$

$$2Al(NO_3)_3\cdot 9H_2O+3CO(NH_2)_2= \\ 2AlO(OH)+6NH_3+6NO_2+3CO_2+17H_2O \tag{4}$$

$$Zr(NO_3)_4\cdot 5H_2O+2CO(NH_2)_2= \\ ZrO_2+4NH_3+4NO_2+2CO_2+2H_2O \tag{5}$$

$$2La(NO_3)_3\cdot 6H_2O+3CO(NH_2)_2= \\ La_2O_3+mNH_4NO_3+(6-m)NH_3+ \\ (6-m)NO_2+3CO_2+(12-m)H_2O \tag{6}$$

Figures 4(a−d) show the morphology of the final reduced powder. Compared with pure molybdenum powder, the molybdenum particles significantly reduce in size after the addition of oxides. Figures 4(a–c) show that the morphology of pure molybdenum (PM), Mo−2.0vol.%Al_2O_3 alloy (MA), and Mo−2.0vol.%ZrO_2 alloy (MZ) powders is microsphere, indicating that the addition of Al_2O_3

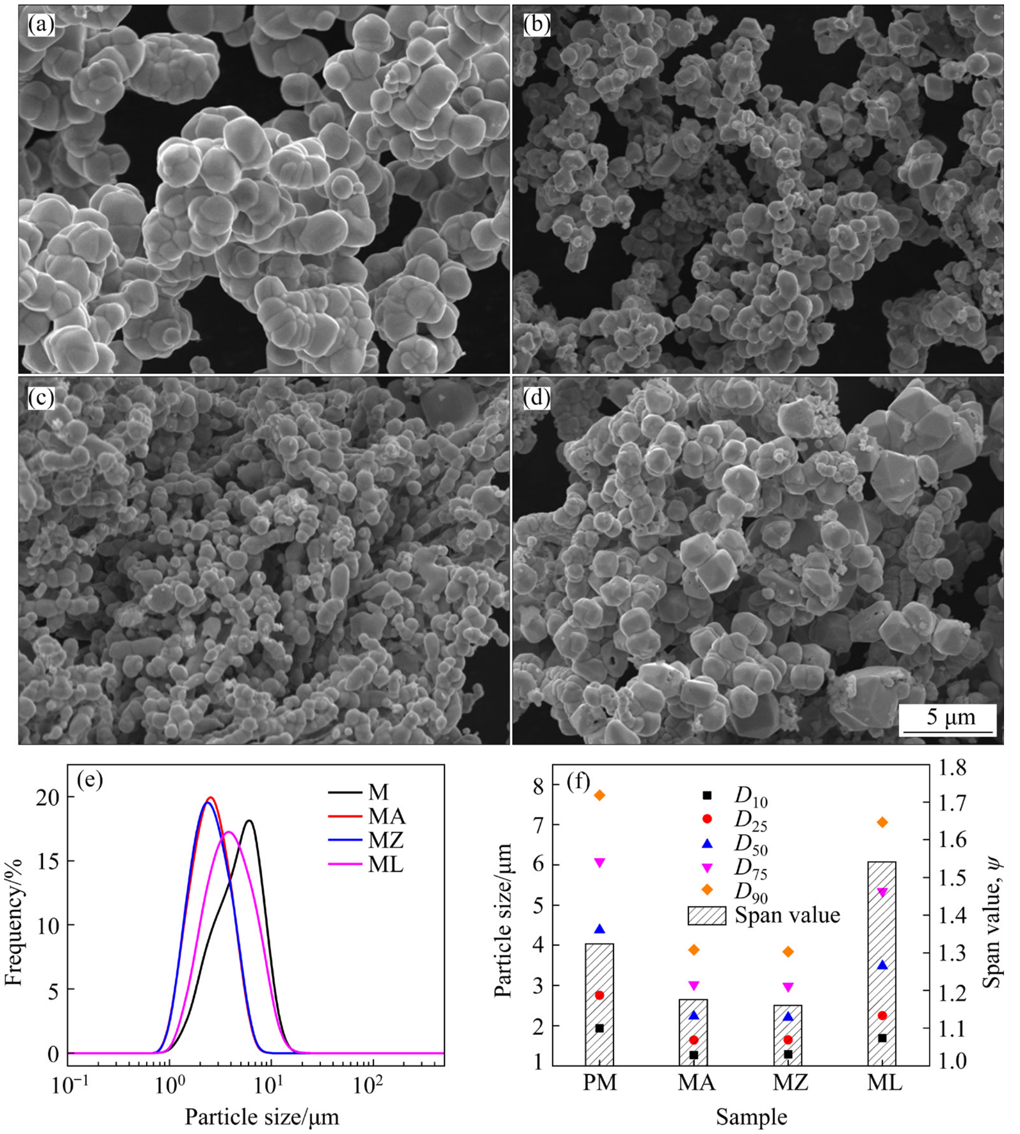

Fig. 4 Morphology and particle size distribution of final reduced powder: (a) PM; (b) MA; (c) MZ; (d) Mo−2.0vol.%La_2O_3 alloy (ML); (e) Size distribution of four powders; (f) Variation trend of particle size distribution parameters of four kinds of powders.

and ZrO_2 particles has little effect on the morphology of the molybdenum matrix. However, the Mo powder doped with La_2O_3 particle is polyhedral (Fig. 4(d)), possibly due to the adsorption of La_2O_3 particles with high surface activity on some of the crystal faces of molybdenum particles; this morphology suggests specific crystal surface growth.

Figure 4(e) illustrates the particle size distributions of four kinds of reduced powders. The size distributions of Mo/Al_2O_3 and Mo/ZrO_2 powders are narrower than those of pure Mo and Mo/La_2O_3 powders, which is consistent with the SEM images (Figs. 4(a−d)). Figure 4(f) depicts the variation trend of particle size distribution parameters (D_{10}−D_{90}) of the four kinds of reduced powders. The mean grain size (D_{50}) of pure Mo, Mo/Al_2O_3, Mo/ZrO_2, and Mo/La_2O_3 powders are 4.383, 2.229, 2.205 and 3.486 μm, respectively. The span value (ψ) is used in describing the uniformity of grain and is calculated by Eq. (7):

$$\psi=(D_{90}-D_{10})/D_{50} \tag{7}$$

The SEM images and particle size analysis show that the average particle size and ψ value of the MZ powder are the smallest, indicating that the doping effect of ZrO_2 is most suitable for the powder preparation process. Meanwhile, the ψ value of ML powders is maximal, which may mean unfavorable grain growth during sintering.

3.2 Microstructures of alloys

Figure 5 shows the microstructures and XRD patterns of the molybdenum alloys. Regrading rotary swaging molybdenum, as shown in Figs. 5(a−d), the grain size of molybdenum alloy becomes finer after the addition Al_2O_3, ZrO_2, or La_2O_3 than pure molybdenum. The reason is that fine oxide particles not only inhibit the growth of molybdenum powder during hydrogen reduction but also pin the grain boundary during sintering, hindering grain boundary flow [23]. The detailed examination of molybdenum grain sizes is shown in Fig. 6(a). The average grain sizes of PM, MA, MZ and ML are 27.3, 5.3, 3.2 and 7.2 μm, respectively. The grain refinement effect of oxide−Mo alloys exceeds 70% than that of pure molybdenum, as shown in Fig. 6(b). After annealing at 1200 °C for 1 h, the grain size of pure molybdenum increases obviously (Fig. 5(e)). The morphology of pure Mo grains changes from irregular at room temperature to equiaxed grains after annealing at 1200 °C. FAN et al [18] pointed out that pure molybdenum recrystallizes completely at 1200 °C. However, the

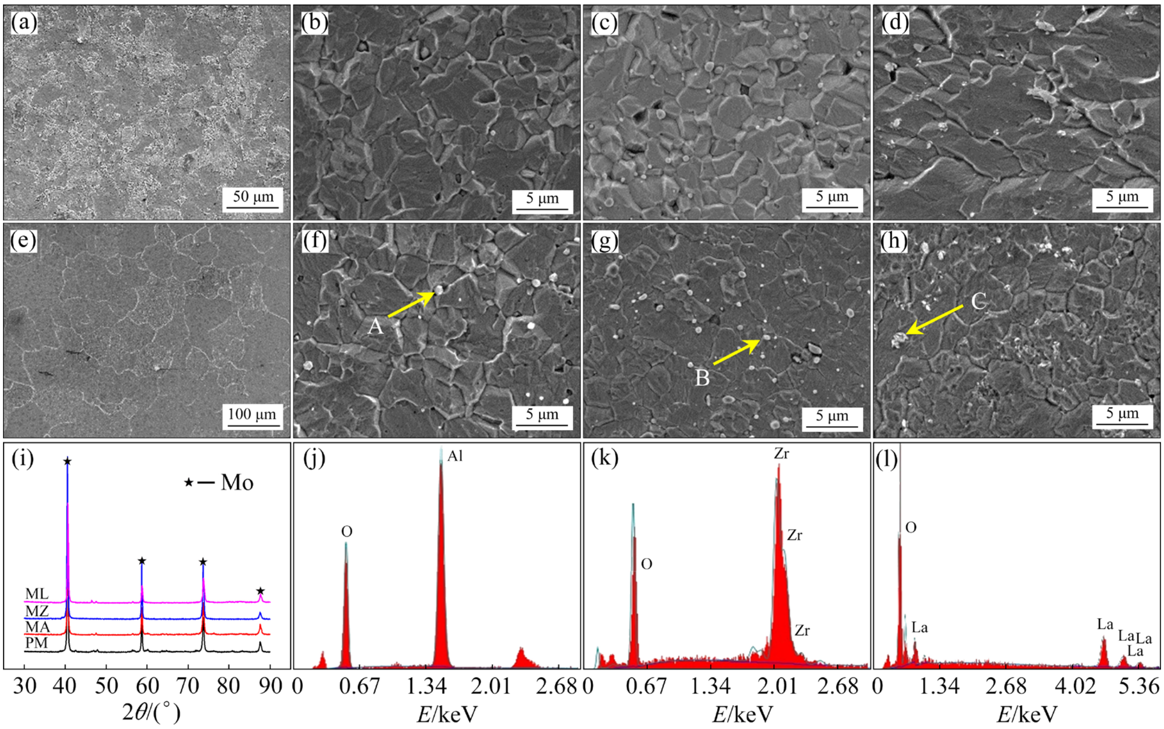

Fig. 5 Microstructure of swaged (a−d) and annealed (e−h) molybdenum alloys: (a, e) PM; (b, f) MA; (c, g) MZ; (d, h) ML; (i) XRD patterns of four swaged molybdenum alloys; (j−l) EDS spectra of corresponding oxides grains

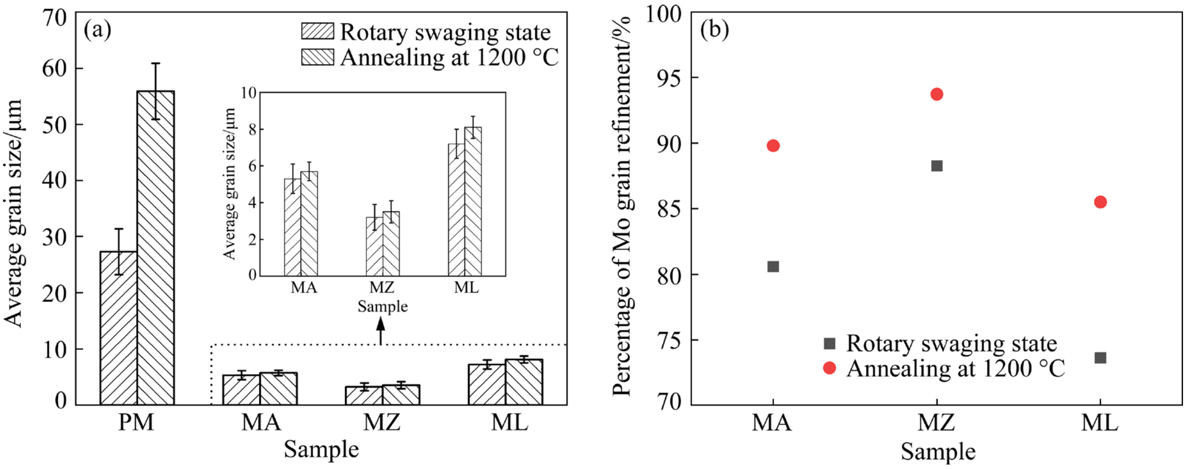

Fig. 6 Statistics of average grain sizes of swaged and annealed Mo matrix (a), and percentage of Mo grain refinement by doping oxide particles

grain sizes of oxide−Mo alloys show slight growth after annealing at 1200 °C (Figs. 5(f−h)), which is observed directly in the inset of Fig. 6(a). The results indicate that the addition of Al_2O_3, ZrO_2, or La_2O_3 particles can improve the recrystallization temperature of molybdenum alloys. Figure 5(i) shows the typical XRD patterns of swaged molybdenum alloys with different oxides. All the peaks in these data correspond to the body-centered cubic polymorphs of molybdenum, but peaks corresponding to oxides are not detected in the XRD patterns, which may be due to the low volume fractions of Al_2O_3, ZrO_2, or La_2O_3 in the molybdenum matrix. The fine bright white particles were marked by Arrows A, B, and C in Figs. 5(f, g, h), respectively, and analyzed through EDS. The results in Figs. 5(j−l) show that these white fine particles correspond to the oxides in Mo−Al_2O_3, Mo−ZrO_2, and Mo−La_2O_3 alloys, respectively.

The morphology and sizes of the oxides in the molybdenum alloys were determined by FESEM, as illustrated in Fig. 7. At least 200 fine Al_2O_3, ZrO_2, or La_2O_3 particles were measured within each alloy with random cross-section by using Image−J software, and the accurate measured value of each molybdenum alloy was obtained. As shown in Figs. 7(a, c), the sphere-shaped Al_2O_3 and ZrO_2 particles are uniformly distributed in molybdenum matrix, and the average grain sizes of Al_2O_3 and ZrO_2 are 48.29 nm (Fig. 7(b)) and 34.54 nm (Fig. 7(d)), respectively. However, determining whether La_2O_3 particles have multiscale sizes and different shapes, as shown in Fig. 7(e), with an average particle size of 68.36 nm (Fig. 7(f)), is interesting. The large aggregates of La_2O_3 particles can be observed in the yellow circle of Fig. 7(e) and caused by two reasons. First, the powder metallurgy process generally does not refine all the La_2O_3 particles to an extremely fine level. Second, in the sintering process, the La_2O_3 particles tend to aggregate because they have higher activity than ceramic oxides [20]. In fact, the morphology and size distribution of a second phase affect all the mechanical properties of molybdenum alloys.

The fine structures of the alloys were characterized by TEM and HRTEM, as shown in Fig. 8. The smaller secondary phase particles are mainly distributed within the molybdenum matrix, and the larger secondary phase particles are mainly distributed at the molybdenum grain boundaries. Obvious dislocation rings are present around the nano-oxide particles, as shown in Figs. 8(a, c, e). The microstructures of molybdenum alloys doped with different oxides, as shown in Figs. 8(b, d, f), are interfaced with the molybdenum matrix. Al_2O_3, ZrO_2, La_2O_3, and Mo have interface width of about 3.3, 3.5, and 3.1 nm, respectively. According to the crystal plane parameters from Figs. 8(b, d, e), the crystal structures of the three oxides are classified as closely packed hexagonal α-Al_2O_3, cubic c-ZrO_2, and cubic c-La_2O_3, respectively. The interface relationship between an oxide and molybdenum phase is usually classified by Bramft's two-dimensional mismatch theory (Eq. (8)) [24]. HU et al [25] pointed out that lattice mismatch $|\delta|<5\%$, $|\delta|=5\%-25\%$, and $|\delta|>25\%$ correspond to the coherent,

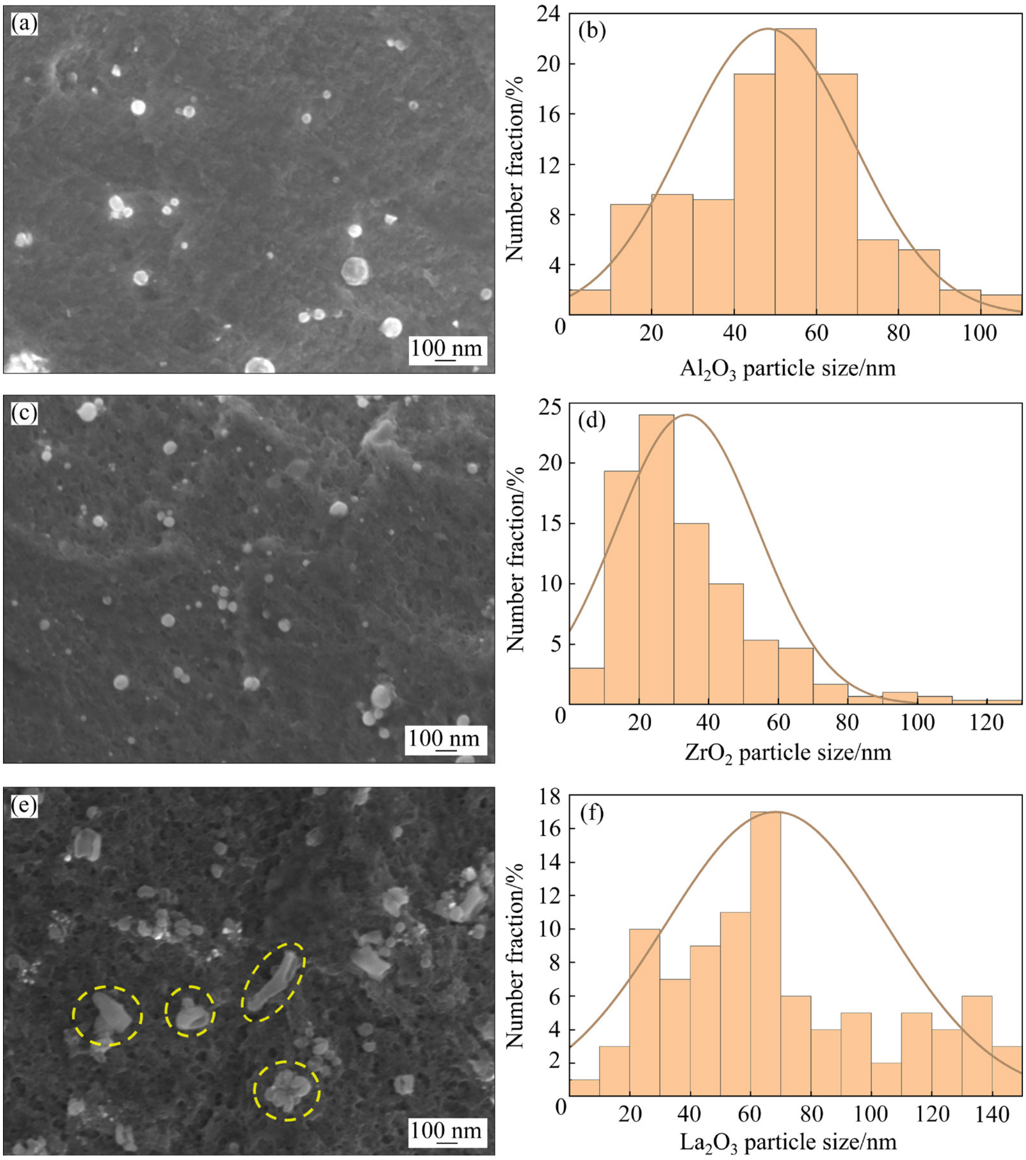

Fig. 7 FESEM images (a, c, e) and oxides particle size distribution (b, d, f): (a, b) Mo−2.0vol.%Al_2O_3; (c, d) Mo−2.0vol.% ZrO_2; (e, f) Mo−2.0vol.%La_2O_3

semi-coherent, and non-coherent interfaces, respectively. According to Eq. (8), the interface mismatch between ZrO_2 and Mo phase is 16.32%, indicating that ZrO_2 has a semi-coherent relationship with the molybdenum matrix on (110) crystal plane, as shown in Fig. 8(d).

$$\delta_{(hkl)_n}^{(hkl)_s} = \frac{|d_{[UVW]_s}\cos\theta - d_{[UVW]_n}|}{d_{[UVW]_n}} \times 100\% \qquad (8)$$

where “s” and “n” mean substrate and nucleated solid, respectively.

3.3 Mechanical properties of alloys

3.3.1 Density, hardness and elastic modulus

Table 1 lists the relative density, Vickers hardness ($HV_{0.2}$), nano-hardness, and elastic modulus of molybdenum alloys. After rotary swaging, the relative densities of the Mo alloys doped with different oxides exceed 98.5%. In general, mechanical properties are improved with increasing alloy density.

In terms of microhardness, the addition of Al_2O_3, ZrO_2, or La_2O_3 significantly improves the microhardness of pure molybdenum, and annealing can decrease the microhardness of molybdenum alloys. The microhardness of rotary swaged Mo alloys doped with Al_2O_3, ZrO_2, or La_2O_3 particles is increased by 25.81%, 36.02%, and 23.12%, respectively, relative to that of pure molybdenum, and the microhardness of annealed state is increased

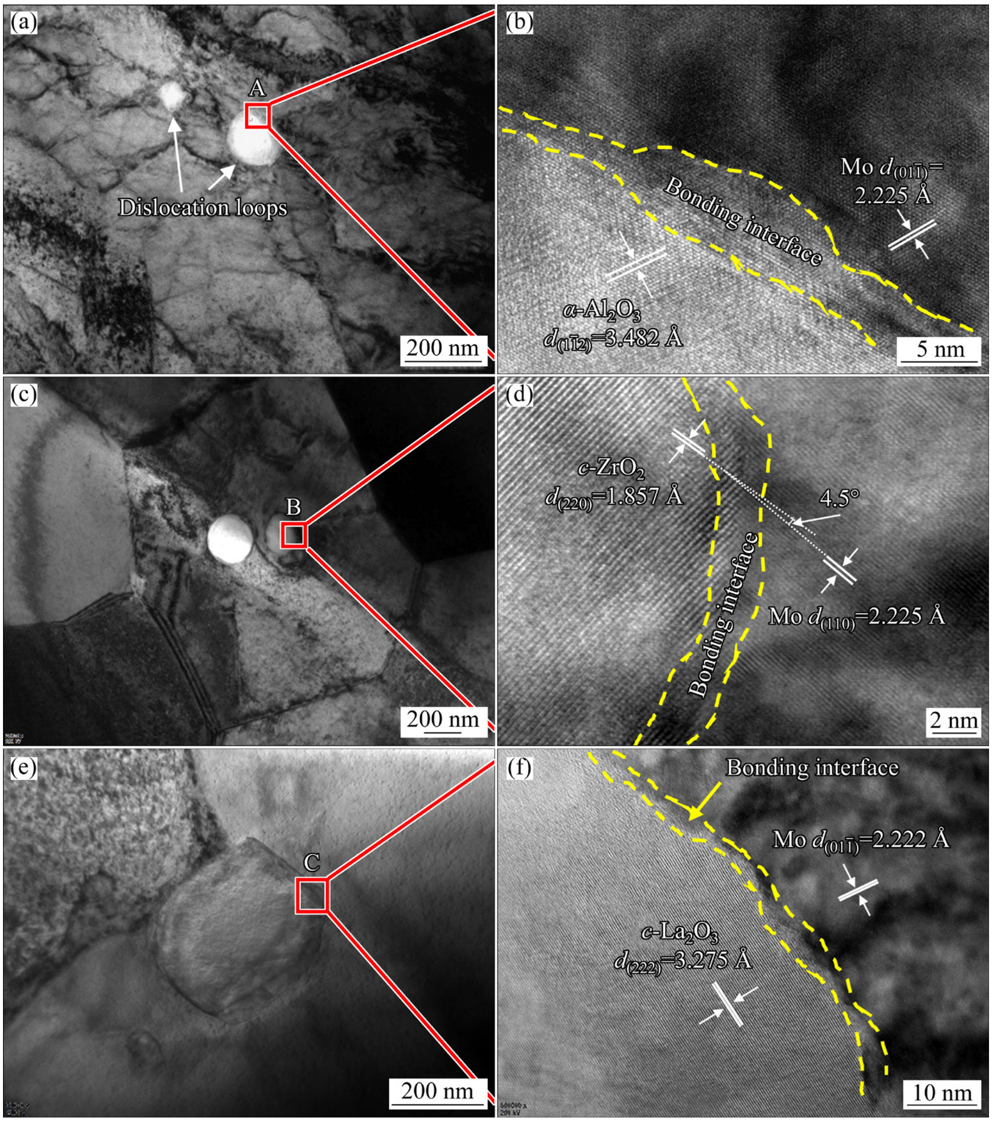

Fig. 8 TEM (a, c, e) and HRTEM (b, d, f) images of molybdenum alloys doped with different oxides: (a, b) Mo−2.0vol.% Al_2O_3; (c, d) Mo−2.0vol.% ZrO_2; (e, f) Mo−2.0vol.% La_2O_3

Table 1 Mechanical properties of rotary swaged and annealed molybdenum alloys

Sample	State	Relative density/%	Vicker hardness ($HV_{0.2}$)	Nano-hardness/GPa	Elastic modulus/GPa
PM	Rotary swaging	95.02	186±7.2	4.15±0.12	314.7±6.0
	Annealing at 1200 °C	–	150±6.5	3.70±0.15	301.0±5.3
MA	Rotary swaging	99.04	234±6.7	4.41±0.10	329.4±4.9
	Annealing at 1200 °C	–	209±6.1	4.35±0.08	325.2±5.7
MZ	Rotary swaging	99.41	253±5.9	4.70±0.08	352.3±5.5
	Annealing at 1200 °C	–	221±4.9	4.42±0.07	329.3±5.0
ML	Rotary swaging	98.75	229±7.1	4.50±0.11	330.7±4.7
	Annealing at 1200 °C	–	201±5.4	4.30±0.08	322.5±5.2

by 39.33%, 47.33%, and 34.00%, respectively. The high microhardness may be related to the following facts. On the one hand, high-density molybdenum alloys have low porosity, which reduces the possibility that micropores become crack sources. On the other hand, dispersed ultrafine oxide particles inhibit dislocation movement, increase the dislocation density of molybdenum matrix and improve the microhardness of molybdenum alloys [26].

Nano-indentation characterization was used in measuring the nano-hardness and elastic modulus of the alloys. This method eliminates the influence of grain boundaries on hardness and directly reflects the influence of microstructure on the micromechanical properties of materials. As given in Table 1, the nano-hardness and elastic modulus of the molybdenum alloys doped with Al_2O_3, ZrO_2, or La_2O_3 particles are higher than those of pure molybdenum, whether in rotary forging or annealing state. MZ alloy has the highest nano-hardness and elastic modulus. In tungsten alloy doped with Al_2O_3 particles, WANG et al [27] pointed out that the high nano-hardness is due to the interaction mechanism between dispersed fine oxides and dislocation movement. Meanwhile, improvement in elastic modulus indicates an increase in rigidity, thus deforming the molybdenum alloy when subjected to external force is difficult.

3.3.2 Tensile properties of molybdenum alloys

The engineering tensile stress–strain curves of pure molybdenum and molybdenum alloys doped with Al_2O_3, ZrO_2, or La_2O_3 are shown in Figs. 9(a, b). The strength and ductility of the molybdenum alloys are significantly improved after the addition of fine oxide particles (Figs. 9(c, d)) and expressed by ultimate tensile strength (UTS), YS and elongation (EL), respectively. In a rotary swaging state, the UTS values of molybdenum alloys increase from 610 MPa (PM) to 644 MPa (MA), 743 MPa (MZ), and 622 MPa (ML). After annealing at 1200 °C, UTS values of molybdenum alloys increase from 511 MPa (PM) to 606 MPa (MA), 703 MPa (MZ), and 586 MPa (ML). Meanwhile, the EL values of swaged MA, MZ, and ML reach 33.7%, 33.8%, 30.4%, respectively, whereas the EL values of the annealed MA, MZ, and ML reach 36.1%, 24.4%, and 37.6%, respectively. Compared with 7.4% and 5.0% of EL values of PM, the improvement is more remarkable. The UTS and EL values of molybdenum alloys doped with different oxides are better than those of most metals and alloys stretched at room temperature [9,12,15,23,28−34], as shown in Fig. 10. In sheet tensile tests, Mo alloy sheet has a high tensile strength, but poor plasticity. Compared with the sheets, the molybdenum alloy bars show

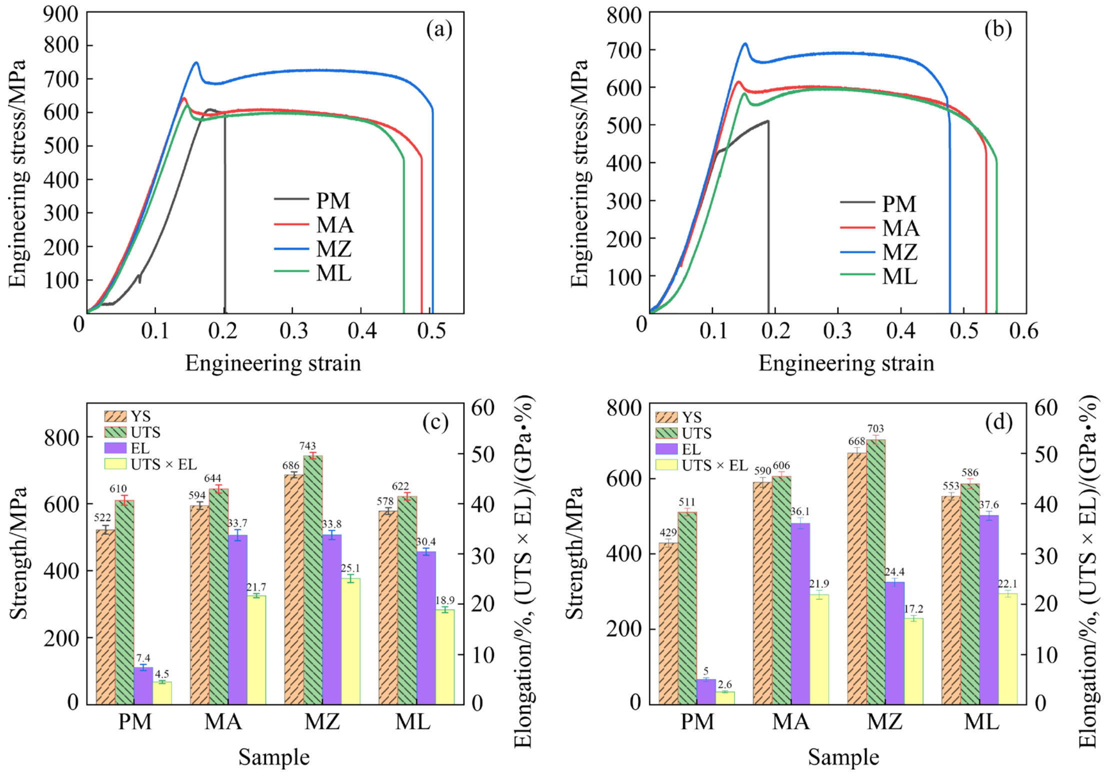

Fig. 9 Mechanical properties of molybdenum alloys: (a) Engineering stress−strain curves of samples in rotary swaging state; (b) Engineering stress−strain curves of samples annealed at 1200 °C; (c) Comparison of YS, UTS, EL and UTS × EL of samples is rotary swaged state, (d) Comparison of YS, UTS, EL and UTS×EL of samples annealed at 1200 °C

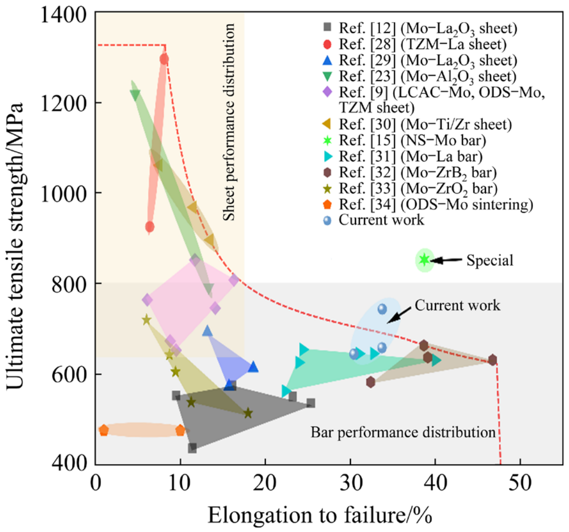

Fig. 10 UTS−EL values distribution of current work in comparison with available literature data of molybdenum alloy sheets or bars at room temperature.

better plasticity, especially in the current work, although the strength is reduced. The satisfactory plasticity and high strength of MA, MZ, and ML are mainly due to the fact that the dispersive ultrafine oxide particles effectively refine molybdenum grains, pin the dislocations, and inhibit crack growth in the Mo matrix. The nanostructured Mo alloy exhibits high strength and excellent room temperature plasticity which is also due to its fine Mo grain size of about 0.5 μm [15].

Notably, the product of the UTS and EL of Mo alloys (i.e., strength–elongation product, UTS × EL, used in characterizing the strength–ductility balance and collision energy absorption in the automotive industry) is greatly influenced by the addition of fine oxide (Figs. 9(c, d)). In the rotary swaged state, the values of UTS × EL increase dramatically from 4.5 GPa·% (PM) to 21.7 GPa·% (MA), 25.1 GPa·% (MZ), and 18.9 GPa·% (ML), by 381%, 456%, and 319%, respectively (Fig. 9(c)). As for the annealed state, the values of UTS × EL increase from 2.6 GPa·% (PM) to 21.9 GPa·% (MA), 17.2 GPa·% (MZ), and 22.1 GPa·% (ML), by 756%, 571% and 762%, respectively (Fig. 9(d)). The UTS × EL values of MA, MZ, and ML surpass those of high-strength TZM alloys.

Meanwhile, the YS of molybdenum alloy is also improved by the addition of oxides. The YS of the rotary swaged state molybdenum alloys (Figs. 9(c, d)), is increased by 13.8% (MA), 31.4% (MZ), and 10.7% (ML), whereas the YS of the annealed state molybdenum alloys is increased by 37.5% (MA), 55.7% (MZ), and 28.9% (ML). Thus, by introducing ultrafine Al_2O_3, ZrO_2, or La_2O_3 particles, the mechanical properties of molybdenum alloys are greatly improved, and the trade-off between strength and ductility is offset. In addition, owing to the random internal defects of MA and ML, their mechanical properties are inferior to those of the MZ alloy.

3.3.3 Tensile fracture surfaces

Figure 11 shows the fracture surfaces of the four samples after rotary swaging. A typical cleavage brittle fracture mode for pure Mo can be observed in Figs. 11(a, a_1), including low magnification fracture and clear river-shaped pattern. An obvious secondary crack indicates that Mo grains are in intergranular fracture mode.

However, after introducing Al_2O_3, ZrO_2, or La_2O_3 particles, the fracture surface morphologies of molybdenum alloys are changed. A mixed failure mode can be observed from the high-power SEM images in Figs. 11(b, c, d), including cleavage fracture, quasi-cleavage fracture, and ductile fracture. The failure surfaces of Mo−Al_2O_3 and Mo−La_2O_3 alloys exhibit relatively plane fracture, whereas the failure surface of Mo−ZrO_2 is inclined by almost 45° along the tensile direction. Compared with Mo−Al_2O_3 and Mo−La_2O_3 alloys (Figs. 11(b_1, d_2)), Mo−ZrO_2 has a smaller dimple size due to the small grain size of matrix, implying a good plasticity (Fig. 11(c_2)). The microstructures are consistent with the stress–strain curves in Fig. 9(a).

Figure 12 shows the tensile fracture morphology of Mo alloys annealed at 1200 °C. Owing to the complete recrystallization of pure molybdenum, large molybdenum grains can be observed on the fracture surface, showing cleavage fracture (Fig. 12(a)). Compared with the swaged pure molybdenum, the failure surface consists of a river-shaped pattern with large cleavage planes and cleavage steps. There are a certain number of pores on the fracture surface of pure molybdenum, which are considered to be a serious defect for metal materials. When the alloy is subjected to external load, these pores form a pre-existing crack source, which eventually hinders the improvement in mechanical strength and ductility.

After the addition of Al_2O_3 and La_2O_3, the fracture modes of the alloys change from brittle

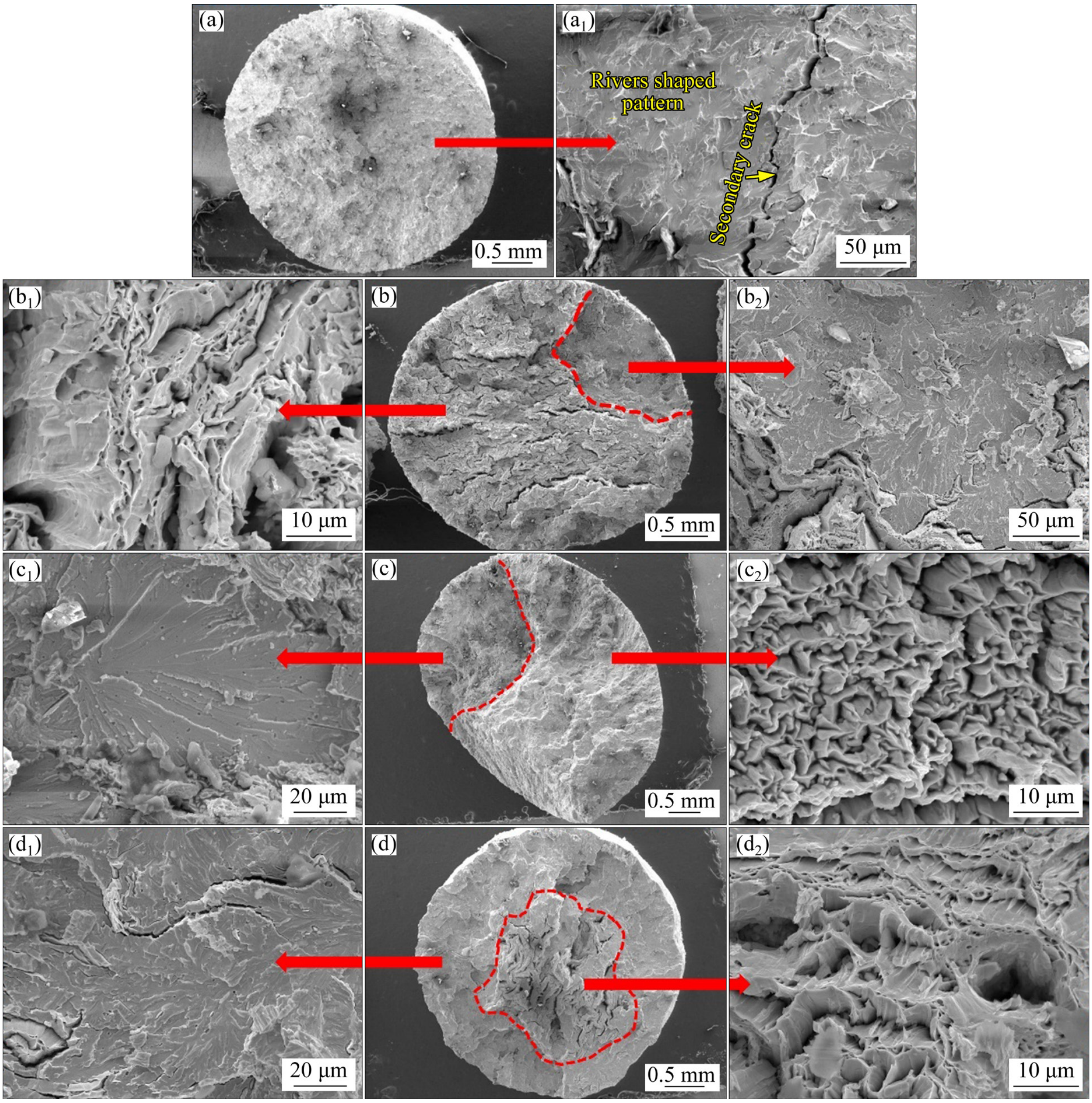

Fig. 11 Fracture morphologies of rotary swaged molybdenum alloys in low power and high power: (a) Pure Mo; (b) Mo−2.0vol.%Al_2O_3; (c) Mo−2.0vol.%ZrO_2; (d) Mo−2.0vol.%La_2O_3: (b_1, c_2, d_2) Ductile fracture zones of corresponding alloy, (b_2, c_1, d_1) Brittle fracture zones

fracture to ductile fracture, and large dimples are formed (Figs. 12(b, d)). The fracture morphology of Mo−ZrO_2 alloy is obviously different from that of Mo−Al_2O_3 and Mo−La_2O_3, showing intragranular fracture, intergranular fracture, and micro-dimples (bright white linear), as shown in Fig. 12(c). This may be attributed to the following reasons. First, ultrafine ZrO_2 particles are uniformly distributed in the molybdenum matrix, which significantly reduces the grain size of Mo, and increases the complexity of the grain boundary, thus inhibiting the plastic deformation of fine Mo grains and producing intergranular fracture. Second, coarse ZrO_2 particles at the grain boundary cause stress concentration and interface debonding at weak grain boundaries, leading to an intergranular fracture mode [19]. However, some Mo grains have intragranular fracture, maybe because ultrafine ZrO_2 particles within Mo grains hinder the movement of dislocations, resulting in a large number of dislocations and crack initiation in Mo grains.

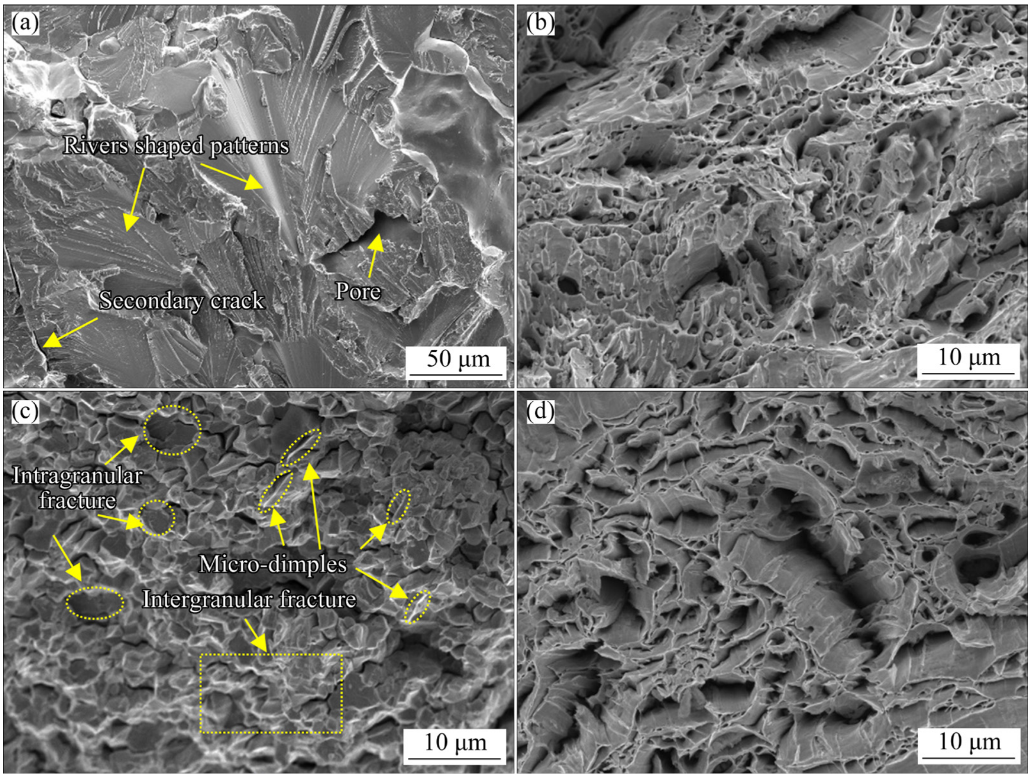

Fig. 12 Tensile fracture surface morphologies of molybdenum alloys annealed at 1200 °C: (a) Pure Mo; (b) Mo−2.0vol.%Al_2O_3; (c) Mo−2.0vol.%ZrO_2; (d) Mo−2.0vol.%La_2O_3

4 Discussion

4.1 Effects of different oxides on microstructure and property

The doping of three kinds of oxides can significantly refine the grain size of molybdenum and increase the recrystallization temperature of molybdenum alloys. The distributions of Al_2O_3 and ZrO_2 particles in the molybdenum matrix are more uniform than the distribution of La_2O_3 (Fig. 7) mainly because La_2O_3 has high surface activity and is easy to agglomerate. MIRZA et al [35] also reported the phenomenon in magnesium alloys with rare earth elements. The three oxides can form good bonding interfaces with molybdenum matrix (Fig. 8). A good bonding interface significantly improves the bonding strength between the secondary phase and molybdenum matrix, thus improving the strength and plasticity of the molybdenum alloy [25]. The semi-coherent relationship between ZrO_2 and Mo phase shows that ZrO_2 has the minimal lattice misfit with the molybdenum matrix. JIANG et al [13] demonstrated that high-density nano-precipitates with the minimal lattice misfit between precipitates and matrix greatly improve the strength of alloy. Therefore, the addition of ZrO_2 particles has the best effect on improving the mechanical properties of molybdenum alloys.

4.2 Strength contribution analysis

The strengthening mechanisms of molybdenum alloys doped with different oxides in this study were discussed in detail. The three main contributions to yield strength are as follows: (1) Grain refinement strengthening (σ_{HP}) can improve alloy strength without losing ductility. Its contribution can be expressed via Hall−Petch relation; (2) dispersion strengthening (σ_{or}) can be analyzed by the Orowan mechanism; (3) dislocation strengthening (σ_D) mainly follows the famous Bailey–Hirsch relation. Thus, the theoretical yield strength (σ_y) of molybdenum alloys can be predicted using Eq. (9):

$$\sigma_y=\sigma_0+\sigma_{HP}+\sigma_{or}+\sigma_D \quad (9)$$

where σ_0 is the intrinsic lattice stress of a large-grained pure molybdenum in the absence of any other strengthening mechanism.

Oxide particles dispersed in a molybdenum matrix hinder dislocation movement, resulting in dislocation loops around the oxide particles (Fig. 8). As external force increases, dislocation movement is intensified and dislocation loops are constantly produced and annihilated. The strengthening effect is expressed by σ_{or}:

$$\sigma_{\mathrm{or}}=\frac{M\mu b}{1.18\times 2\pi\varphi\left(\sqrt{\pi/6f}-1\right)}\ln\left(\frac{\varphi}{2b}\right) \tag{10}$$

where M is the Taylor factor with a value of 2.5 for the body-centered cubic crystal structure, and μ is the shear modulus with a value of 140 GPa for molybdenum alloy [18]. The oxide particle sizes (φ) are listed in Table 2 according to Fig. 7, and the volume fraction of oxide particles is considered the original addition of 2.0%. The σ_{or} values are calculated via Eq. (10) and listed in Table 2.

Table 2 Orowan strength of swaged molybdenum alloys

Sample	Oxide particle size, φ/nm	Oxide volume fraction/%	Orowan strength, σ_{or}/MPa
MA	48.29	2	26.8
MZ	34.54	2	37.5
ML	68.36	2	18.9

During the tensile deformation, a large number of dislocations move in the molybdenum matrix and gather at the grain boundaries, which leads to work hardening and dislocation strengthening effect. Through Bailey–Hirsch analysis, the dislocation strengthening can be quantitatively expressed by Eq. (11) [36]:

$$\sigma_{\mathrm{D}}=\alpha M\mu b\sqrt{\rho} \tag{11}$$

where α is a geometric factor taken as 0.28 [36] and ρ is the dislocation density estimated using XRD patterns (Fig. 5(i)). The values of ρ are calculated via Eqs. (1) and (2) and σ_{D} are listed in Table 3.

Table 3 Dislocation strength of swaged molybdenum alloy doped with different oxides

Sample	Micro-strain, ε	Crystallite size, d/μm	Dislocation density, ρ/m^{-2}	Dislocation strength, σ_{D}/MPa
MA	0.131	1.14	1.5×10^{15}	10.2
MZ	0.144	0.92	2.0×10^{15}	11.9
ML	0.117	1.82	8.2×10^{14}	7.7

According to the Hall–Petch relationship, the grain refinement strengthening σ_{HP} can be described as follows:

$$\sigma_{\mathrm{HP}}=\sigma_0+\frac{K}{D^{1/2}} \tag{12}$$

where K is the Hall−Petch constant and D is the grain size. The values of σ_0 and K can be determined from the intercept and slope of liner profile fit of the (σ_y−σ_{or}−σ_{D}) versus $D^{-1/2}$, respectively, as shown in Fig. 13. According to the fitting result, σ_0 and K are 361 MPa and 485 MPa·μm$^{-1/2}$, respectively. Therefore, the contribution values (σ_{HP}) of the grain refinement strengthening are calculated using Eq. (12). The results are shown in Table 4.

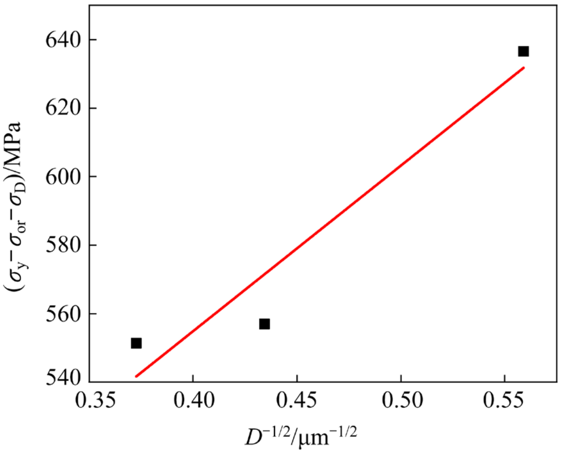

Fig. 13 Hall−Petch relationship curve between stress and molybdenum grain sizes

Table 4 Grain refinement strength of swaged molybdenum alloy doped with different oxides

Sample	Grain refinement strength, σ_{HP}/MPa
MA	210.7
MZ	271.1
ML	180.8

Figure 14 shows the estimated strengthening contributions of dislocation, dispersion, and grain refinement to YS of molybdenum alloys doped with different oxides. Grain refinement strengthening plays a dominant role in all strengthening mechanisms for molybdenum alloys, contributing 79.7%, 78.3%, and 82.7% to the total yield strength of three molybdenum alloys, respectively. The sum of theoretical calculation values is in good agreement with experiment data. The slight differences may be caused by the following reasons. First, the strengthening mechanisms have not been fully considered, such as deformation strengthening. Second, the theoretical calculation is based on the ideal state of materials, ignoring micropores and impurities. Finally, the superposition law of dislocation, dispersion and grain refinement strengthening cannot be described by simple linear addition, because each strengthening mechanism is not independent of the deformation process [15,37].

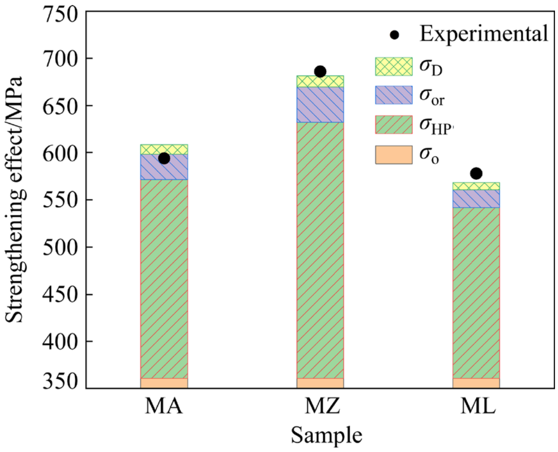

Fig. 14 Estimated strengthening contributions of dislocation, dispersion and grain refinement strengthening mechanisms in yield strength of molybdenum alloys doped with different oxides

5 Conclusions

(1) Composite powders and alloy rods of molybdenum doped with oxides were successfully prepared by hydrothermal synthesis, co-precipitation and co-decomposition, powder metallurgy and swaging.

(2) Most of oxide particles in molybdenum alloy are about tens of nanometers, and the average grain sizes of Al_2O_3, ZrO_2 and La_2O_3 particles are 48.29, 34.54 and 68.36 nm, respectively. These oxides are fine and uniformly distributed in the molybdenum matrix, which refines the Mo grains. The grain refining rate of Mo exceeds 70%.

(3) The YS of molybdenum alloy is improved by the addition of oxides. Compared with pure molybdenum, the YS of rotary swaged Mo alloys is increased by 13.8% (Mo−Al_2O_3), 31.4% (Mo−ZrO_2) and 10.7% (Mo−La_2O_3), while that of annealed state Mo alloys is increased by 37.5% (Mo−Al_2O_3), 55.7% (Mo−ZrO_2) and 28.9% (Mo−La_2O_3).

(4) The strengthening mechanisms of the molybdenum alloy consist of dislocation, dispersion and grain refinement strengthening. Quantitative analyses indicate that the grain refinement strengthening plays a dominant role in all strengthening mechanisms for molybdenum alloys, which accounts for 79.7%, 78.3%, 82.7% of total strengthening contribution for the three molybdenum alloys.

Nomenclatures

YS: Yield strength
UTS: Ultimate tensile strength
EL: Elongation
UTS × EL: Strength−elongation product
ρ: Dislocation density
ε: Micro-strain
b: Magnitude of Burger vector
d: Crystallite size
θ: Bragg diffraction angle
λ: Wave length of Cu K_α
δ_s: Structure broadening
ψ: Span value describing uniformity of grain
δ: Lattice mismatch
PM: Pure molybdenum
MA: Mo−2.0vol%Al_2O_3 alloy
MZ: Mo−2.0vol%ZrO_2 alloy
ML: Mo−2.0vol%La_2O_3 alloy
σ_y: Theoretical yield strength
σ_{HP}: Grain refinement strengthening
σ_{or}: Dispersion strengthening
σ_D: Dislocation strengthening
σ_0: Intrinsic lattice stress of very large-grained pure molybdenum in the absence of any other strengthening mechanism

Acknowledgments

This work was supported by the National Natural Science Foundation of China (Nos. U1804124, U1704152).

References

[1] MILEIKO S T. High temperature molybdenum matrix composites [J]. Ceramics International, 2019, 45(7): 9439−9443.

[2] LUO Ming, FAN Jing-lian, CHENG Hui-chao, TIAN Jia-min. Annealing behavior of rotary forging Mo−Ti−Zr alloy bars [J]. The Chinese Journal of Nonferrous Metals, 2010, 20(5): 866−871. (in Chinese)

[3] WEI Shen-yu, JI Li-na, WU Wen-jie, MA Hong-lin. Selective laser melting of lanthanum oxide-reinforced

tungsten composite: Microstructure and mechanical properties [J]. Tungsten, 2022, 4(1): 67−78.

[4] KIM J M, HA T H, PARK J S, KIM H G. Oxidation resistance of Si-coated TZM alloy prepared through combined process of plasma spray and laser surface melting [J]. Transactions of Nonferrous Metals Society of China, 2016, 26(10): 2603−2608.

[5] SUN Tie-long, XU Liu-jie, WEI Shi-zhong, PAN Kun-ming, LI Wu-hui, ZHOU Yu-cheng, HUANG Zhi-min. Microstructure and compression properties of fine Al_2O_3 particles dispersion strengthened molybdenum alloy [J]. Transactions of Nonferrous Metals Society of China, 2020, 30(12): 3307−3321.

[6] MANNHEIM R L, GARIN J L. Structural identification of phases in Mo−Re alloys within the range from 5 to 95% Re [J]. Journal of Materials Processing Technology, 2003, 143/144: 533−538.

[7] SILLER M, LANG D, SCHATTE J, KNABL W, CLEMENS H, MAIER-KIENER V. Interaction of precipitation, recovery and recrystallization in the Mo−Hf−C alloy MHC studied by multipass compression tests [J]. International Journal of Refractory Metals and Hard Materials, 2018, 73: 199−203.

[8] CHAUDHURI A, BEHERA A N, SARKAR A, KAPOOR R, RAY R K, SUWAS S. Hot deformation behaviour of Mo-TZM and understanding the restoration processes involved [J]. Acta Materialia, 2019, 164: 153−164.

[9] COCKERAM B V. The mechanical properties and fracture mechanisms of wrought low carbon arc cast (LCAC), molybdenum-0.5pct titanium-0.1pct zirconium (TZM), and oxide dispersion strengthened (ODS) molybdenum flat products [J]. Materials Science and Engineering A, 2006, 418: 120−136.

[10] HU Ping, ZUO Ye-gai, LI Shi-lei, XING Hai-rui, HAN Jia-yu, GE Song-wei, HUA Xing-jiang, WANG Kuai-she, ZHANG Wen, FU Jing-bo. Synthesis and oxygen evolution mechanism of hypoxia carbon-control titanium-zirconium-molybdenum alloy [J]. Journal of Alloys and Compounds, 2021, 870: 159429.

[11] LUO Lai-ma, ZHOU Yu-fen, ZHANG Yu-xiang, ZAN Xiang, LIU Jia-qin, ZHU Xiao-yong, WU Yu-cheng. Current status and development trend of toughening technology of molybdenum-based materials [J]. The Chinese Journal of Nonferrous Metals, 2019, 29(3): 525−537. (in Chinese)

[12] CHENG P M, ZHANG G J, ZHANG J Y, LIU G, SUN J. Coupling effect of intergranular and intragranular particles on ductile fracture of Mo−La_2O_3 alloys [J]. Materials Science and Engineering A, 2015, 640: 320−329.

[13] JIANG Sui-he, WANG Hui, WU Yuan, LIU Xiong-jun, CHEN Hong-hong, YAO Meng-ji, GAULT B, PONGE D, RAABE D, HIRATA A, CHEN Ming-wei, WANG Yan-dong, LU Zhao-ping. Ultrastrong steel via minimal lattice misfit and high-density nanoprecipitation [J]. Nature, 2017, 544: 460−464.

[14] SILVA E Z, KESTLER H, SANDIM H R Z. Particle-stimulated nucleation of recrystallization in the hot-deformed molybdenum alloy MZ-17 [J]. International Journal of Refractory Metals and Hard Materials, 2018, 73: 74−78.

[15] LIU G, ZHANG G J, JIANG F, DING X D, SUN Y J, SUN J, MA E. Nanostructured high-strength molybdenum alloys with unprecedented tensile ductility [J]. Nature Materials, 2013, 12(4): 344−350.

[16] CHEN Xuan, LI Bin, WANG Tao, LI Rui, WANG Juan, REN Shuai, ZHANG Guo-jun. Strengthening mechanisms of Mo−La_2O_3 alloys processed by solid-solid doping and vacuum hot-pressing sintering [J]. Vacuum, 2018, 152: 70−77.

[17] XU Liu-jie, WEI Shi-zhong, ZHANG Dan-dan, LI Yan, ZHANG Guo-shang, LI Ji-wen. Fine structure and interface characteristic of α-Al_2O_3 in molybdenum alloy [J]. International Journal of Refractory Metals and Hard Materials, 2013, 41: 483−488.

[18] FAN Xiao-man, XU Liu-jie, WEI Shi-zhong, YAO Li-ying, SUN Tie-long, ZHOU Yu-cheng, PAN Kun-ming, XIAO Fang-nao, SUN Kai. Mechanical properties and strengthening mechanism of the hydrothermal synthesis of nano-sized α-Al_2O_3 ceramic particle reinforced molybdenum alloy [J]. Ceramics International, 2020, 46(8): 10400−10408.

[19] XU Liu-jie, LI Zhou, XIAO Fang-nao, ZHAO Yun-chao, ZHOU Yu-cheng, WEI Shi-zhong. Properties and microstructure of oxide dispersion strengthened tungsten alloy prepared by liquid-phase method: A review [J]. Tungsten, 2023, 5(4): 481−502.

[20] SUN Tie-long, XU Liu-jie, WEI Shi-zhong, XIAO Fang-nao, LI Zhou, FAN Xiao-man, ZHOU Yu-cheng. Phase evolution of hydrothermal synthesis oxide-doped molybdenum powders [J]. International Journal of Refractory Metals and Hard Materials, 2020, 86: 105085.

[21] WILLIAMSON G K, SMALLMAN R E. III. Dislocation densities in some annealed and cold-worked metals from measurements on the X-ray Debye−Scherrer spectrum [J]. Philosophical Magazine, 1956, 1(1): 34−46.

[22] WILLIAMSON G K, HALL W H. X-ray line broadening from filed aluminium and wolfram [J]. Acta Metallurgica, 1953, 1(1): 22−31.

[23] ZHOU Yu-cheng, WEI Shi-zhong, XU Liu-jie, LI Xiu-qing. Research on high-temperature properties of the molybdenum sheet doped with 1.0 wt.%Al_2O_3 particles [J]. Journal of Alloys and Compounds, 2018, 769: 340−346.

[24] BRAMFITT B L. The effect of carbide and nitride additions on the heterogeneous nucleation behavior of liquid iron [J]. Metallurgical Transactions, 1970, 1: 1987−1995.

[25] HU Bo-liang, WANG Kuai-she, HU Ping, SU Yu-tong, LI Shi-lei, XING Hai-rui, HAN Jia-yu, GE Song-wei, HUA Xing-jiang, FU Jing-bo, CHANG Tian. Effect of secondary phases on the strength and elongation of a novel Mo−TiC−ZrC−C alloy [J]. International Journal of Refractory Metals and Hard Materials, 2020, 92: 105336.

[26] WU Zhuang-zhi, ZHAO Na, LU Yao, LIU Hai-lang, DUAN Bo-hua, LIU Xin-li, WANG De-zhi. Effects of shape and size of second phase on mechanical properties of sintered Mo−Y_2O_3 alloys [J]. Transactions of Nonferrous Metals Society of China, 2022, 32(6): 1926−1934.

[27] WANG Chang-ji, ZHANG Lai-qi, PAN Kun-ming, WEI Shi-zhong, WU Xiao-chao, LI Qing-kui. Effect of Al_2O_3 content and swaging on microstructure and mechanical properties of Al_2O_3/W alloys [J]. International Journal of Refractory Metals and Hard Materials, 2020, 86: 105082.

[28] HU Ping, HU Bo-liang, WANG Kuai-she, SONG Rui, YANG Fan, YU Zhi-tao, TAN Jiang-fei, CAO Wei-cheng, LIU Dong-xin, AN Geng, GUO Lei, YU Hai-liang. Strengthening and elongation mechanism of lanthanum-doped titanium−zirconium−molybdenum alloy [J]. Materials Science and Engineering A, 2016, 678: 315−319.

[29] WANG Lin, LIU Gang, SUN Jun. Effects of La_2O_3 and annealing temperature on grain size and mechanical properties of Mo alloys [J]. Materials Research Express, 2017, 4(11): 116515.

[30] CUI Chao-peng, GAO Yi-min, WEI Shi-zhong, ZHANG Guo-shang, ZHOU Yu-cheng, PAN Kun-ming, ZHU Xiang-wei, GUO Song-liang. The mechanical properties of the Mo−0.5Ti and Mo−0.1Zr alloys at room temperature and high temperature annealing [J]. High Temperature Materials and Processes, 2017, 36(2): 167−173.

[31] YANG Xiao-qing, TAN Hua, LIN Nan, LI Zhi-xiang, HE Yue-hui. Effects of the lanthanum content on the microstructure and properties of the molybdenum alloy [J]. International Journal of Refractory Metals and Hard Materials, 2016, 61: 179−184.

[32] ZHANG Guo-jun, ZHUO Jun, REN Shu-ai. Microstructure and mechanical properties of molybdenum alloys doped with ZrB_2 particles [J]. Advanced Materials Research, 2010, 160/161/162: 1828−1833.

[33] CUI Chao-peng, ZHU Xiang-wei, LI Qiang, ZHANG Min, ZHU Guang-ping, LIU Shu-long. Study on high temperature strengthening mechanism of ZrO_2/Mo alloys [J]. Journal of Alloys and Compounds, 2020, 829: 154630.

[34] COCKERAM B V. The fracture toughness and toughening mechanism of commercially available unalloyed molybdenum and oxide dispersion strengthened molybdenum with an equiaxed, large grain structure [J]. Metallurgical and Materials Transactions A, 2009, 40(12): 2843−2860.

[35] MIRZA F A, WANG K, BHOLE S D, FRIEDMAN J, CHEN D L, NI D R, XIAO B L, MA Z Y. Strain-controlled low cycle fatigue properties of a rare-earth containing ME20 magnesium alloy [J]. Materials Science and Engineering A, 2016, 661: 115−125.

[36] YANG Hui-long, KANO S, SHEN Jing-jie, MCGRADY J, ZHAO Zi-shou, DUAN Zhen-gang, ABE H. On the strength-hardness relationships in a Zr−Nb alloy plate with bimodal basal texture microstructure [J]. Materials Science and Engineering A, 2018, 732: 333−340.

[37] OSETSHKY Y. Strengthening of tungsten by coherent rhenium precipitates formed during low fluence irradiation [J]. Tungsten, 2022, 4(1): 20−27.

不同超细氧化物掺杂钼合金棒材的拉伸性能及强化机理

徐流杰[1,2]，孙铁龙[1]，周玉成[2]，李 洲[3]，魏世忠[1]

1. 河南科技大学 河南省高温结构与功能材料重点实验室，洛阳 471003；
2. 河南科技大学 金属材料磨损控制与成型技术国家地方联合工程研究中心，洛阳 471003；
3. 中国机械科学研究总院 北京机科国创轻量化科学研究院有限公司，北京 100089

摘 要：通过水热合成、共沉淀、共分解、粉末冶金和旋锻方法制备了 3 种掺杂 2.0%(体积分数)不同氧化物(Al_2O_3、ZrO_2和La_2O_3)的钼合金棒材。3 种纳米氧化物均使钼晶粒细化 70%以上，且使合金的断裂模式从脆性断裂转变为韧性断裂，从而显著提高钼合金的综合力学性能，克服强度和韧性之间的矛盾。在 3 种钼合金中，Mo−ZrO_2合金具有最佳的强度和塑性，这归因于细小的ZrO_2颗粒以及ZrO_2与钼基体之间的半共格界面。此外，建立了与位错密度、氧化物体积分数和尺寸以及钼晶粒尺寸相关的定量强化模型。

关键词：钼合金；Al_2O_3；ZrO_2；La_2O_3；强塑积；强化模型

(Edited by Bing YANG)